Role of device architecture and AlOX interlayer in organic Schottky diodes and their interpretation by analytical modeling

Role of Device Architecture and Oxidized Aluminum Nanostructures as Charge Transport Interlayer in Organic Schottky Diodes; Interpreting the Physical Phenomena with Analytical Modeling

Nikita Kumari,[1,a)] Manish Pandey,[1,b)] Kengo Hamada,[1] Daisuke Hirotani,[1] Shuichi Nagamatsu,[2] Shuzi Hayase,[1] Shyam S. Pandey[1,a)]

[1]*Graduate School of Life Science and Systems Engineering, Kyushu Institute of Technology, 2-4 Hibikino, Wakamatsu, Kitakyushu, 8080196 Japan*

[2]*Department of Computer Science and Electronics, Kyushu Institute of Technology, 80-4 Kawazu, Iizuka, 820-8502 Japan*

Considering the pivotal role of interfaces in controlling the performance of organic electronic devices, implications of metal/organic interfacial quality in Schottky barrier diode (SBD) is investigated. Nature of metal/organic interfaces and thin film quality of regioregular poly (3-hexylthiophene) (RR-P3HT) based SBDs fabricated in different device architectures is investigated using both of the experimental and theoretical approaches. Importance of oxidized aluminum nanostructures as inter-layer at Schottky interface for the dramatic enhancement of the rectification ratio ($>10^6$ at $\pm$ 5V) has been demonstrated, which is attributed to suppressed leakage current due to the oxide layer and the formation of charge double layer. Furthermore, electrical performances of all the SBDs were modeled in terms of underlying particular phenomenon solely or with the combination of multiple physical phenomena. The combined modeling equation used in this work fits well for the different device architectures, which validates its generality in order to extract the device parameters.

[a)] **Author to whom correspondence should be addressed. Electronic mail:** shyam@life.kyutech.ac.jp**;** nikita.jisce@gmail.com

[b)] Present address: *Graduate School of Materials Science, Nara Institute of Science and Technology, Ikoma, Nara, 630-0192 Japan*

Keywords: Organic Schottky Diode; Thermionic Emission; Space Charge Limiting Current; Trap States, Conjugated Polymer; Analytical Modeling.

I. INTRODUCTION

The emergence of solution processable semiconducting conjugated polymers (CPs) with diverse synthetic versatility and introduction of various functional groups for controllable optoelectronic properties have led to their vast applications in organic electronic devices.[1–6] Advent of CPs have made it possible to fabricate devices under the ambient conditions, however, undesired doping and trap states should be controlled efficiently for performance reproducibility.[7–10] In spite of the significant efforts that has been made in the past to interpret and solve these issues, there exist a big room for the improvement. Performance of the CP based electronic devices depends on the bulk (quality of organic thin film) and interfaces (contact resistance at the junctions). Interfacial band structure is responsible for the contact resistance (R_C), which can be tuned by the choice of metal, CP and interlayer; however, presence of trap states is well known to play a dominant role in deciding the R_C.[11–15] In this regard, Tsukagoshi and coworkers reported that in spite of lower work function of copper (Cu) with higher hole injection barrier at the Cu/pentacene interface, resultant R_C with Cu top contact was smaller than corresponding Gold (Au) contact.[12] Ideally, in the organic field effect transistors (OFETs), if there exist a barrier for hole injection at source contact then there should not be any barrier for hole extraction at drain contact considering the similar band structure. Since R_C at both the interfaces are reported to be of the same order, therefore, dominance of the trap states in R_C cannot be denied.[13] In this regard, not only interfacial trap states are responsible for R_C, the presence of trap states in bulk of the film arising at the boundaries also play a crucial role, which stringently depends on the film crystallinity.[9,16–18] Bulk resistance (R_B) inversely depends on the film crystallinity because with decrease in film crystallinity effective carrier mobility decreases[19] and current in forward bias (when applied forward bias (V_a) exceeds the built-in voltage (V_{bi})) is governed by well-known

Mott-Gurney relation regarding space charge limited current (SCLC).[20–23] There are numerous reports in which the physical phenomena occurring in the organic diodes were interpreted by comparing the experimental observations through theoretical models. These models were developed considering the bulk phenomena (SCLC or drift current region) and the interface dependent charge injection phenomena (at the Ohmic contact), either one at a time or by combined effect as a function of applied voltage.[7,24–28] However, device structure dependent deviation of the physical model from practical electrical characteristics still remains a chalange.[26,29,30] Here in we are reporting a general/robust model considering the whole interface and bulk phenomena of an organic Schottky barrier diode (OSD), irrespective of the device architecture.

In this work, OSDs were fabricated with different interfacial structure and film morphology. Their electrical characteristics were analyzed to investigate the combined effect of interface and bulk on the device performance in terms of thermionic emission and Mott-Gurney SCLC equations. Schottky diodes consist of a semiconductor layer placed between the Ohmic and Schottky contacts, which allow injection and blocking of the current flow under the forward and reverse biasing, respectively.[31] Resultant rectification ratio (RR) of the diode depends on the nature of Schottky contact, and large Schottky barrier is desired for high RR. Since most of the CPs in pristine state show p-type behavior, which reflects the relative carrier mobility in the organic layer; therefore, low work-function cathode such as calcium, magnesium, etc. is recommended to block hole injection efficiently under reverse bias. Although they provide larger Schottky barrier with decrease in work-function, their air-stability also decreases resulting in to rapid device deterioration.[32] Thus to achieve optimum device performance, Aluminum (Al) was chosen as electrode material to make Schottky contact with poly (3-hexylthiophene) (P3HT) and Ohmic contact was formed utilizing Au.[33] On oxidation, work-function of Al decreases unlike other

metals, and this exceptional property was exploited to improve RR of the OSDs.[34–36] Presence of a thin oxidized Al (AlO_X) interlayer between P3HT and Al led to investigate its influence on the electrical characteristics of the OSDs. AlO_X layer formed on the CP film under similar conditions was also characterized through atomic force microscopy (AFM), X-ray and ultraviolet photoelectron spectroscopy (XPS and UPS) for better interpretation of its effect on the OSD's electrical characteristic. Further, the effect of film crystallinity on the device performance was also investigated and for that, films were cast by the two different methods such as spin-coating and drop-casting, which provided different film crystallinity as verified by grazing incidence X-ray diffraction (GIXD) measurement. This work deals with investigations pertaining to the implications of the AlO_X interlayer and film crystallinity on the device performance along with the analysis of the observed results through different modeling equations. The modeling equations were designed by integrating the possible physical phenomena occurring in the device at the electrode/organic interfaces and inside the bulk (CP film).

II. Experimental Section

A. Materials and Device fabrication

Electronic grade regioregular P3HT and super dehydrated chlorobenzene were purchased from Sigma Aldrich and used as received. P3HT was dissolved in chloroform (1.5% w/w) and chlorobenzene (0.2% w/w) to fabricate thin films by spin-coat and drop casting, respectively. Metal deposited glass substrates were used for device fabrication. Drop-casted films were prepared by dropping the polymer solution on metal patterned substrates covered with petri-dish to facilitate slow solvent evaporation. On the other hand, spin-coated films were prepared at spin speed of 800 rpm for 5 s followed by 1500 rpm for 40 s. Both types of P3HT films were fabricated under ambient

conditions and then vacuume (~10^{-3} Torr) dried for 30 min. Then films were annealed at 150 ℃ for 20 min in argon atmosphere followed by thermal evaporation of top metal pads under high vacuum (below 10^{-6} Torr) using shadow masks. In this work, OSDs with cross-sectional area 4 mm^2 (except when it is mentioned) were fabricated using P3HT as the active semiconductor while thermally evaporated Al and Au metal were utilized for making Schottky and Ohmic contacts, respectively. The OSDs were fabricated in three different device architectures such as with Al as top contact with and without AlO_X interlayer and Au as top contact as shown in **Figure 1**. In the case, when OSDs were fabricated with AlO_X interlayer (Figure 1 (b)), at first a thin (10 nm) Al layer was thermally evaporated on P3HT under high-vacuum followed by exposing them to ambient condition for ~ 1 hour to facilitate the oxidation of Al forming AlOx. Later, 60 nm thick Al was thermally evaporated on AlO_X under high vacuum to complete the device fabrication. It is worth mentioning here that this 10 nm of AlO_X layer was not continuous as characterized by AFM and will be discussed later.

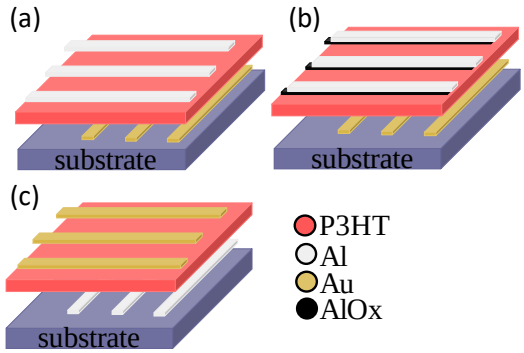

FIG. 1. Schematic illustration of the device architectures with top Al contact pristine (a) and with AlO_X interlayer (b) and with Al contact at the bottom (c).

B. Characterization

Electrical characterizations (current – voltage) of the OSDs were performed using a source-measure unit (Keithley 2612). For the estimation of switching speed of the OSDs, output voltage of the OSD was measured by placing it in series with a load resistor (2 kΩ) and a variable frequency AC-voltage source (Multi-Function Generator, WF1974). An oscilloscope (Agilent MSO-X 2004A) was connected across the resistor to monitor the ripple voltage. GIXD (in-plane and out-of-plane) measurements of similar spin coated and drop casted P3HT films were carried with Rigaku smart Lab. Photoelectron spectroscopy (XPS and UPS) measurements were performed using Shimadzu Kratos Axis-Nova spectrometer. Al Kα excitation source was used at pass energy of 80 eV with the energy resolution of 1000 meV. Samples of XPS and UPS characterization were prepared by thermal evaporation of 10 nm of Al on top of the P3HT film and they were kept in ambient conditions for 1 h before the measurement. Depth profiling by XPS and UPS was also conducted by etching with Ar^+ ions for different time intervals varying from 0-60 s. The AFM images of similarly prepared films were obtained using a scanning probe microscope (JSPM5200, Shimadzu, Japan).

III. RESULTS AND DISCUSSION

A. Current-Voltage Characteristics of OSDs

The current density-voltage ($J-V$) characteristic of OSDs fabricated in different device architectures are shown in **Figure 2** (a). This asymmetric $J-V$ characteristic clearly reveals the facile flow of current in the forward bias and blocking of current in the reverse bias conditions, which can be attributed to the formation of Schottky barrier at the Al/P3HT interface. Thermionic

emission model as given in Eq. 1 was proposed for inorganic Schottky diodes but it has been widely accepted for organic semiconductors as well.[21,33,37,38]

$$J = J_0 \left[\exp\left(\frac{qV}{\eta kT}\right) - 1\right] \quad (1)$$

Where,

$$J_0 = A^* T^2 \exp\left(-\frac{q\phi_B}{kT}\right) \quad (2)$$

Where, J and V represent current density and applied voltage, respectively. The constant terms are A^* (Richardson constant), k (Boltzmann constant), T (ambient temperature) and q (electronic charge). η, J_0 and ϕ_B are device parameters representing ideality factor, reverse saturation current density and barrier height respectively. J_0 and η were calculated from the intercept and slope of $\ln J-V$ plot and the RR was calculated from the ratio of current flowing through the device under forward and reverse bias at the same applied potential. All of the calculated parameters for different devices structures are summarized in **Table I**. Asymmetric $J-V$ characteristics with high RR is among the most important criterion for a practical diode. Therefore, state-of-art work reported by other groups in the literature is also listed in **Table II** for the comparison. A perusal of Figure 2 and Table I clearly corroborates that RR of the OSD having pristine Al top contact is similar to that of devices in Al as bottom contact (in the order of 10^4). This can also be understood from the statistical distribution of $J-V$ characteristics of multiple devices of each type as shown in **Figure S1 and Table SI (Supplementary Information)**.

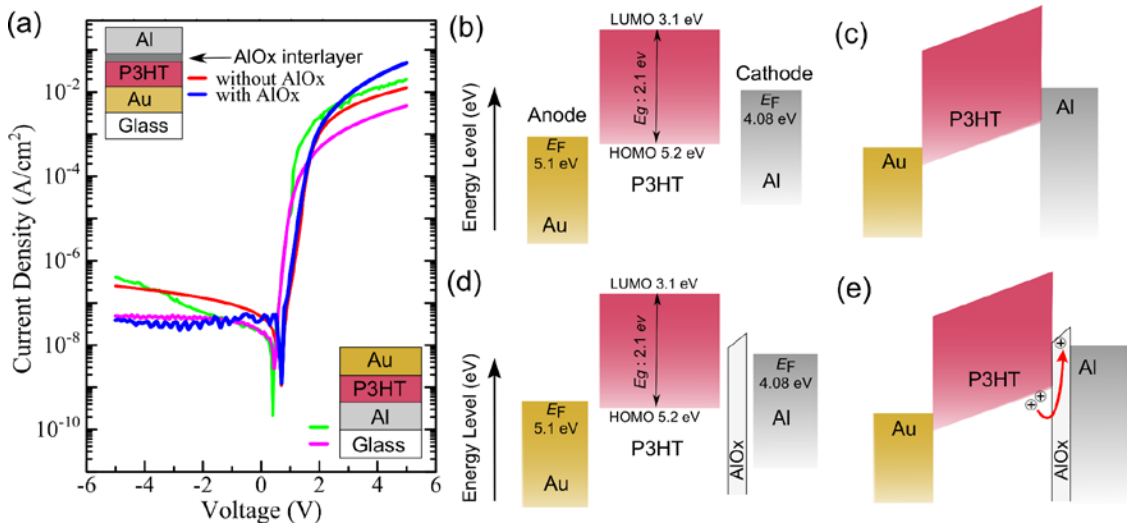

FIG. 2. $J-V$ characteristics of the Schottky diodes (a) along with the device architectures shown in the inset. Energy band diagram for the different layers in the OSD with pristine Al and AlO_X interlayer (nano-structures of AlO_X with the 10 nm thick Al) at the Schottky contact (b, d) and Energy band diagram of the corresponding OSDs in forward bias ($V_a > V_{bi}$) (c, e). Energy levels are shown with respect to the vacuum level.

Interestingly, there was a remarkable enhancement in the RR (~ 2 orders of magnitude) of the OSD with top Schottky contact having an interfacial layer of AlO_X (with optimized thickness of 10 nm as shown in **Figure S2**). This enhancement in RR can be attributed to the optimal interfacial band structure at the Schottky contact. Upon oxidation, the work function of Al decreases at the Schottky interface,[34] which favors the holes transport under forward bias but blocks in the reverse direction leading to enhancement in the ON-current (I_{on}), while OFF-current (I_{off}) was reduced more effectively. Low RR was observed for OSDs with Al at bottom, where the formation of thin oxide layer at the interface in ambient condition naturally occurs. Therefore, the effect of device architecture on the performance of OSDs was also probed in detail. Since the pristine Al surface cannot oxidize fully, therefore, an arbitrary state 'x' is considered to represent the oxidized Al layer (AlO_X) and its corresponding work-function was drawn less than that of pristine Al in Figure

2 (d,e). The oxide growth saturates towards depth due to limited penetration of aerial oxygen irrespective of the exposer time and it has been reported to be ~2 nm for Al. Nonetheless, the work-function of AlO_X also starts to increase with ageing.[34] Considering both of these points, the interfacial Al layer was exposed to the ambient condition for 1 h. Schematic representation of energy band structure of the OSDs with and without AlO_X layer has been shown in Figure 2(b-e). The increasing trend of work-function of AlO_X towards the depth of interfacial layer represents the lesser oxidized region. To construct the energy band diagram, the work functions of Au and Al, along with the energy of highest occupied molecular orbital (HOMO) and lowest unoccupied molecular orbital (LUMO) of P3HT was taken from the literature.[39,40] After the inception of CPs and demonstration of their semiconducting behavior, Schottky model based on thermionic emission developed for the silicon has been quite frequently used straightway for the organic diodes to deduce electronic parameters like ideality factor.[41] Standard Schottky model predicts that the depletion region should be confined to the small part of the film thickness. However, in OSDs, low carrier concentration leads to the extension of depletion region throughout the film thickness ($\approx$100 – 200 nm). This poses limitation to the straightforward use of thermionic emission model for OSDs leading to the proposal of other models like metal-insulator-metal (MIM) without having partial depletion region.[27,42–44] This was further validated through small value of experimentally calculated Richardson constant (2×10^{-9} $Acm^{-2}K^{-2}$) obtained by temperature dependent $J-V$ characteristics of OSDs, which is far from the typical value of Richardson contestant (120 $Acm^{-2}K^{-2}$) used for inorganic semiconductors.[33,45] Keeping these arguments in mind, energy band diagram for the OSD as shown in Figure 2 (c, e) was constructed considering the MIM model.

TABLE I. Electronic parameters calculated for the OSDs fabricated in different device architectures. AFM image (Figure 3) shows nanostructures of AlO_X for the corresponding thickness of 10 nm of Al shown by thickness monitor.

Diode configuration	**Rectification ratio (RR)** (at $V = \pm 5$ V)	**Ideality factor (η)**
Al-top contact (without AlO_X)	$4.01 \times 10^4 \pm 32.23\%$	$1.48 \pm 15.2\%$
Al-top contact (with 10 nm AlO_X)	$1.11 \times 10^6 \pm 14.63\%$	$1.70 \pm 33.8\%$
Al-bottom contact	$4.73 \times 10^4 \pm 57\%$	$1.48 \pm 10.5\%$

Contrary to OSDs fabricated with Al top contact as shown in Figure 1, $J-V$ characteristics were noisy and suffered with the reproducibility issues with Au top contact as shown in Figure 2(a) and Figure S1. The non-repetitive $J-V$ curves in combination with pronounced leakage current for OSDs with Au top contact could be attributed to the diffusion of heavy and hot Au atoms into the soft polymeric semiconductor film. Which is supposed to cause large Au–thiol chemical interaction and damaged Au/P3HT interface.[46,47]

TABLE II. Summary of previously published characteristics of organic Schottky diodes and recent progress of printable inorganic Schottky diode is also included for comparison

Structure	**RR**	***J* (A/cm^2); corresponding V (V)**	**Publication year**	**Reference**
Cu/CuTCNQ/pentacene/Al	2×10^6	0.51; 5	2010	[48]
Au/PEDOT:PSS/P3HT/Al	3×10^4	0.1; 3	2009	[49]
Cu/PTAA/Ag	10^5	~ 0.1; 5	2011	[15,50]

Cr/Au/C_{16}IDT-BT/MoO_3/Ag	$> 10^6$	~ 5; 5	2017	[51]
Pt/InGaZnO/Al	2.2×10^4	0.65; 1	2016	[52]
Ti/Pd/InGaZnO/Mo	10^8	300; 1	2013	[53]
Au/P3HT/AlO_X/Al	(1.11×10^6 ± 14.63%); at ± 5V	(0.053 ± 28.75%); 5	This work	

B. Morphological characterization

In order to visualize the surface morphology of the optimized AlO_X interlayer (10 nm), AFM measurement was conducted and the obtained images are shown in **Figure 3**. From the perusal of Figure 3 (a, b), small islands of Al (≈ 100 nm wide) was clearly observed from the height image with root mean square (RMS) surface roughness of ≈ 2.61 nm. Minimization of surface energy might have assisted this formation of islands during thermal evaporation since the metal deposition occurs as a tiny cluster of atoms. Moreover, less freedom to rearrange themselves on the polymer surface could also have assisted the formation of such nanostructured interface. This can be understood by the fact that when the similar or even lower thickness of Al was coated on bare Si/SiO_2 substrate in same deposition condition, continuous Al film was observed as shown in **Figure S3.** Despite the fact that islands partially cover the underneath polymer layer (≈30%, as shown in **Figure S4**), the RR for the OSDs with AlO_X interlayer was found to be dramatically improved compared to that of devices without AlO_X interlayer with Al at top (Figure 2 (a)). As already stated, oxidation of the exposed surface of Al continues up to around 2 nm in depth, but the nano-islands of AlO_X play a dominant role in the device performance due to increase in their effective surface area. When the Al surface is exposed to air, a large amount of oxygen is also

expected to be trapped on the oxide surface. The empty levels of the adsorbed oxygen are filled by the electron tunneling from the underlying Al atom, concomitantly a charge double layer is formed with a negative charge on the external surface as schematically shown in Figure 3(c). It can also be noticed that resultant electric field due to this charge double layer assist the hole transport in the forward direction; however, it hinders the hole transport with Al at bottom contact as shown in Figure 3(c). Thus it can be said that the optimum thickness of AlO_X interlayer is controlled by three parameters, which are the optimum coverage of the underlying CP layer, the presence of pristine Al below the AlO_X layer for charge double layer formation and the distance of the charge double layer from the underlying CP layer for optimum effect on the charge transport. It is worth to note here that during optimization, thickness shown by the Quartz crystal monitor was considered without commenting on its continuity but considering its effect on the $J-V$ characteristics. Therefore, from now on, this thickness value will be used for the device nomenclature.

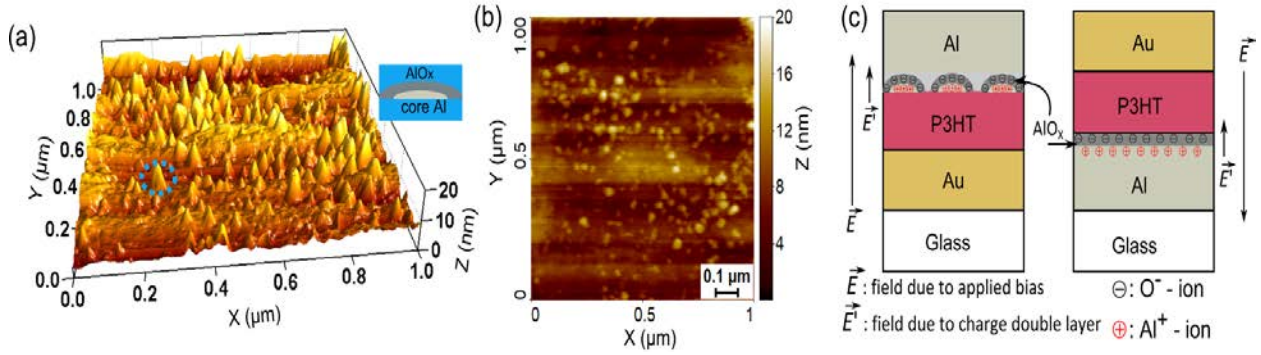

FIG. 3. AFM images of the 10 nm oxidized Al deposited on top of the spin-coated P3HT film exhibiting height (a) and phase (b) images. Inset of (a) depicts the schematic for partially oxidized Al-island. (c) Schematic representation for the formation of charge double layer due to adsorbed oxygen on AlO_X layer.

C. Interfacial characterization

To have in-depth insight about interfacial chemical composition and electronic band structure of AlO_X on P3HT, XPS and UPS depth profiling was conducted with the sample as shown schematically in **Figure 4** (a). Wide-energy XPS spectrum for the sample is shown in Figure 4 (b) exhibiting peaks corresponding to Al 2p, Al 2s, C 1s and O 1s at binding energy of 75 eV, 120 eV, 287 eV and 533 eV, respectively. A similar XPS profile for wide scan of AlO_X layer generated upon variously oxidized Al surfaces has also been reported by Gupta et al.[54] Presence of the weak XPS peak corresponding to C 1s along with peaks corresponding to O 1s and Al 2p is attributed to the presence of hydrocarbon impurity at the surface of oxidized Aluminum (AlO_X).[55] Complete disappearance of C 1s peaks just after 10 s of Ar^+ ion etching from top further supports the presence of hydrocarbon impurity. It can be seen in the Figure 4 (d, e) that as a function of etching time (i.e. sample depth), there is an increase in the counts of Al 2p and concomitantly decrease in the O 1s atomic peak indicating a relative reduction in the extent of AlO_X. In XPS measurement, the incident source was of very high energy (1486.6 eV), therefore, the obtained signal contains the corresponding peaks of elements present up to ~ 5 – 10 nm depth.[35] Since the height of Al-islands are also of the same order (rms surface roughness ≈ 2.61 nm as observed in AFM measurement), therefore, change in the ratio of the XPS signal corresponding to Al 2p and O 1s was considered for probing the AlO_X layer formed after the aerial oxidation of Al.

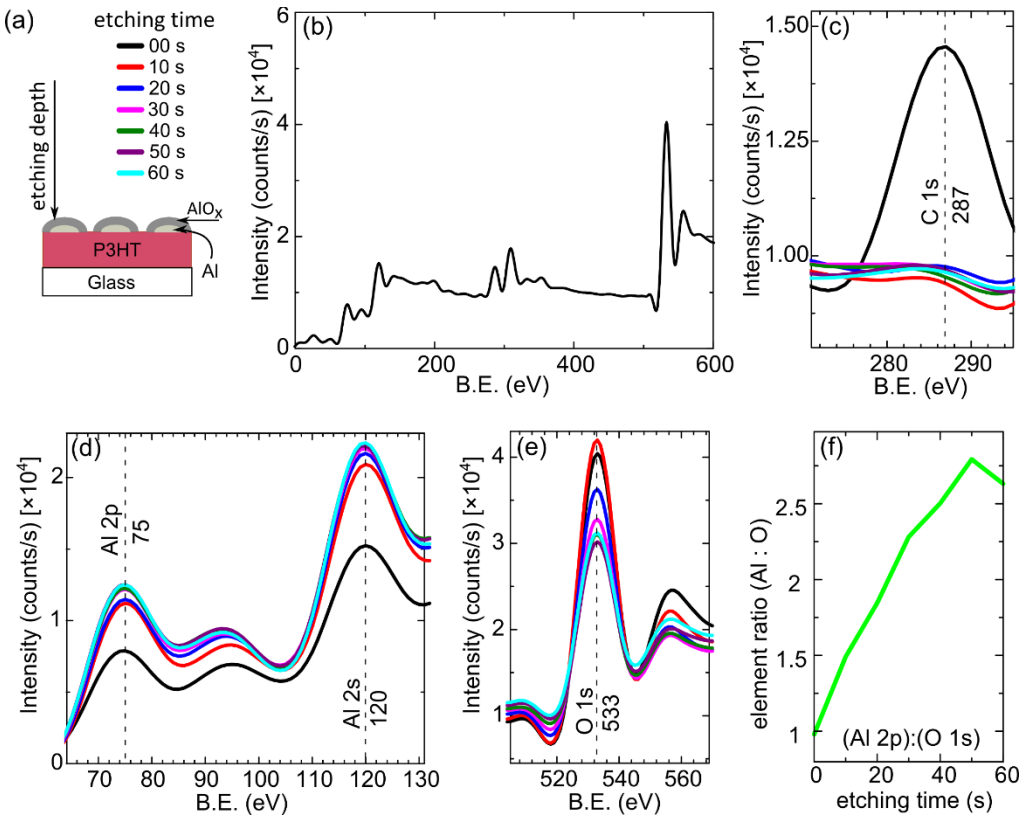

FIG. 4. (a) Schematic representation of sample geometry used for the depth profiling of AlO_X interlayer by XPS and UPS and the inset shows the set of ligands corresponding to graphs in (b – e). (b) Wide scan XPS spectral profile before etching and narrow scan elemental profiling with Ar^+ ion etching from top for (c) Carbon, (d) Aluminum and (e) Oxygen. (f) Probing AlO_X interlayer represented in terms of ratio of percentage contribution in XPS spectrum corresponding to Al 2p and O 1s as a function of etching time.

A perusal of Figure 4(f) clearly corroborates that initially Al 2p to O 1s ratio was increasing, which corresponds to a decrease in oxygen contents with depth followed by a decrease after 50 sec of etching. Although only limited penetration of oxygen is possible inside the Al islands, some amount of oxygen is always present in the underlying polymer film due to its processing under ambient conditions, therefore, Al 2p peak intensity decreases after certain depth but that of O 1s saturates which might be the reason for the decrease in Al to O ratio (Figure 4 (f)).

The sample was further subjected to UPS measurement before and after consecutive Ar^+ ion etching from the top and the obtained results are shown in **Figure 5**. In the UPS spectra at the secondary electron cutoff position (corresponding spectra magnified in right inset), the binding energy of the sample decreases with depth. They were found at the binding energy of 17.81 eV, 17.81 eV, 17.65 eV and 17.45 eV for 0 s, 20 s, 40 s and 60 s of sample etching, respectively. The valence band edge (represented by the intersecting lines) shifts towards higher energy with increase in sample etching and were found to be 4.24 eV, 4.83 eV, 4.90 eV and 4.90 eV for samples before and after 20 s, 40 s and 60 s of etching, respectively. These shifts correspond to an increase in the work-function of the AlO_X interlayer, which has been shown schematically in the band diagram after inserting the AlO_X layer in Figure 2 (e).[35]

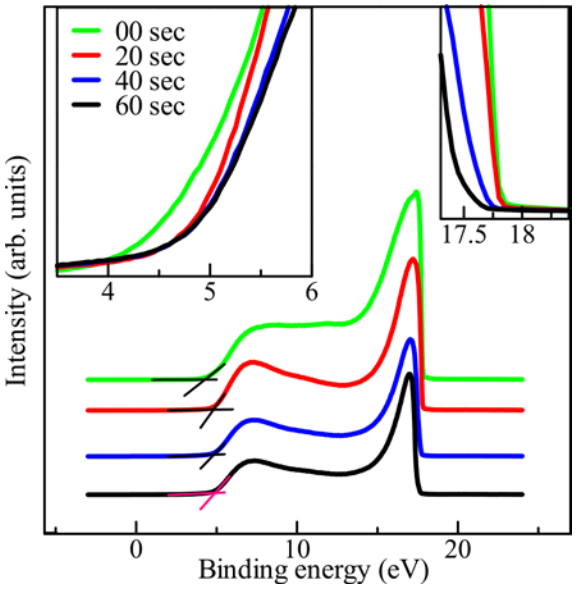

FIG. 5. UPS spectral profile for AlO_X island layer on P3HT before and after Ar^+ ion etching (Incident beam energy (He–I) = 21.2 eV). Sample geometry for this was also the same as shown in the Figure 4 (a).

D. Microstructural characterization

Encouraged by implication of device architecture on the performance of OSDs, where bottom Au and top Al contacts having 10 nm of AlO_X-islands gave the best device performance, effort was directed to examine the influence of film crystallinity and macromolecular conformation on the performance of OSDs. To accomplish this, OSDs were fabricated in the optimized device architecture using thin films of P3HT prepared by spin-coating and drop-casting as described in experimental section. The obtained $J-V$ characteristics along with device architecture used are shown in **Figure 6** (a) and the device parameters obtained by fitting the linear region of $\ln J-V$ characteristics are summarized in **Table III**. It can be clearly seen that in spite of having similar device architecture and fabrication conditions, OSDs having spin-coated thin films exhibited improved device performance as compared to the case of drop-casted thin films.

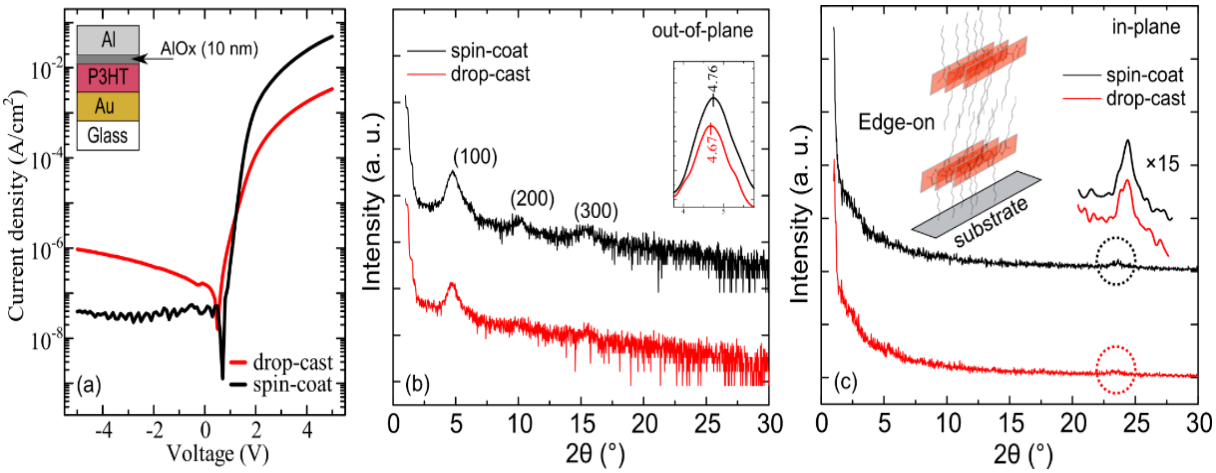

FIG. 6. (a) J - V characteristics of OSDs fabricated using thin films of P3HT prepared by spin-coated and drop-casted films along with the device structures shown in the insets. (b) Out-of-plane and (c) in-plane GIXD pattern for spin-coated and drop-casted films of P3HT. Inset of (b) shows the enlarged view of 100 peak in both the cases. Inset of (c) shows 15 times resolved peak of the in-plane GIXD pattern and schematic representation for edge-on conformation of P3HT molecules.

TABLE III. Electronic parameters calculated for the OSDs fabricated using spin coated and drop cast P3HT films in the device configuration Al-(top)/AlO_X (10 nm)/P3HT/Au-(bottom).

P3HT thin film fabrication method	**d-spacing (Å)**	**Rectification ratio (RR)** (at $V = \pm 5$ V)	**Ideality factor (η)**
Spin-coating	16.95	$1.11 \times 10^6 \pm 14.6\%$	$1.70 \pm 33.8\%$
Drop-casting	17.34	$3.04 \times 10^3 \pm 17.9\%$	$3.28 \pm 18.5\%$

In order to understand such a marked difference in the device performance for the P3HT thin films fabricated by spin-coating and drop-casting methods, these films were subjected to out-of-plane and in-plane GIXD measurements. As can be seen in Figure 6 (b) that in out-of-plane mode GIXD spectra, all the peaks corresponding the lamellar-stacking of the alkyl side-chains appeared at 4.75°, 9.97° and 15.29°. The *d*-spacing calculated from the difference between *100* and *200* peak positions was found to at 16.95 Å and 17.34 Å for the spin-coated and drop-casted P3HT films, respectively. A small shift in *100* peak position ($2\theta \approx 0.1°$) towards the lower angle in drop-casted film also corresponds to increase in *d*-spacing, i.e., the alkyl side-chains are more stretched as compared to the spin-coated one, which causes hindrance in out-of-plane charge transport. From the Figure 6(b), it can also be clearly seen that all the peaks corresponding to the lamella formation via alkyl side-chain stacking were more pronounced up to higher orders for the films prepared using spin coating as compared to the drop-casting method. In general, the position of the peak represents the lamellar stacking distance, whereas the sharpness of the peak is associated with the crystallinity and grain size. Therefore, it can be concluded that in the present case the spin coated films possessed higher degree of crystallinity as compared to that of the drop-casted films. Moreover, in the in-plane GIXD pattern, the presence of peak corresponding to π-π stacking at $2\theta = 23.17°$ and absence of any (*h00*) peaks related to alkyl-stacking in both of the films clearly

suggest the edge-on conformations of the polymeric backbones on the substrate as schematically shown in the inset of Figure 6(c).

Since the thickness of the films prepared by both the methods were of the same order (≈ 200 nm), it is worth mentioning here that films prepared by spin coating by two-successive spin speed were of high crystallinity as compared to the drop-casted method. The edge-on conformation and high-crystallinity of the spin-coated samples prepared here is attributed to the low spin-speed (800 rpm) in combination with relatively higher polymer concentration (2% w/w), which gave enough time to the macromolecules to obtain thermodynamically favored conformation as reported earlier.[16,56–58] At the same time, spin coated films possess high film uniformity with minimum surface roughness due to the absence of coffee ring effect, the drop-casted film possess non-uniform thickness distribution. Due to presence of coffee ring effect, the dissolved polymer molecules moves towards the edges of the drop-casted area, which lead to inhomogeneity in dried film.[59,60] When the top electrode is deposited, diffusion of metal in the pinholes leads to short resistive path resulting in increased I_{OFF} as depicted in Figure 6(a). Since devices were processed in ambient conditions, therefore, due to high surface roughness at the metal/organic interface, effective surface area for gas-adsorption would increase leading to an increase in interfacial trap states.[8] These effects could have played a dominant role in the relatively hampered device performance of OSDs with drop-casted film. Other than these, the bulk resistance due to SCLC, which depends on film crystallinity also affect the $J-V$ characteristics. It is also worth to mention here that unlike planar devices such as OFET, charge transport in the vertical devices like diodes and solar cells ideally takes place in the out-of-plane direction, therefore, a good crystallinity in the transverse direction is required. Otherwise when the charge carrier enters in the bulk of

semiconducting thin film it has to spend larger amount of time inside the film due to increase in intermolecular hopping and scattering centers at grain boundaries before being collected at the other electrode.[9] The charge carriers residing in the organic film creates space charge, applying repulsive force for further charge injection and with increase in charge carrier inside the film the resultant repulsive force increases, interpreted as SCLC.

E. Analytical Modeling

In the ideal OSDs, under forward bias there should not be any injection barrier but practically it is present due to formation of charge accumulation region in the organic thin film near Ohmic contact and the charge carriers overcome this barrier through thermionic emission effect.[28,43] Therefore, under forward bias, $J-V$ characteristics of an OSD is analyzed through comparing it with the approximated thermionic emission model as written in Eq. 3 (approximation of Eq. 1 for $V > (3kT/q)$).[21,33,37,38]

$$J = J_0 \left[\exp\left(\frac{qV}{\eta kT}\right)\right] \tag{3}$$

Using Eq. 3, J_0 is obtained by extrapolating the linear part of the $\ln J-V$ plot to $V = 0$ V, where the value of η is obtained from its slope with the help of Eq. 4. The deviation of η from the ideal value (= 1) can be attributed to the occurrence of tunneling phenomena or scattering of the charge carriers due to presence of trap states in the devices along with the interfacial non-uniformity.[7,21]

$$\eta = \frac{q}{kT}\frac{\mathrm{d}V}{\mathrm{d}(\ln J)} \tag{4}$$

The above discussed model was originally proposed for inorganic devices, thus before generalizing it for organic device, it should be scrutinized extensively. In this regard, calculation of η is an appropriate example which can be calculated from either of the two linear regions with distinguishable slopes present in the $\ln J-V$ plots as shown in **Figure 7**. The higher slope value (present at lower voltage region) is expected to provide the lower value of η. The same trend was followed in the present case as well to obtain the device parameters as summarized in Table-I,III.[61] To verify the calculated physical parameters, corresponding regions on linear scale $J-V$ plot were analyzed as shown in the inset of Figure **7**. It is clear that in higher voltage region, the thermionic emission phenomena is reflected through non-linear region in $J-V$ plot (red color segment in the inset of Figure **7**) and device parameters obtained from this region is summarized in **Table SIII**. Furthermore, to understand the correlation between the device parameter and electrical characteristic, thorough analysis of $J-V$ curve has to be done through a general physical equation, which can incorporate all physical phenomena occurring in the device.

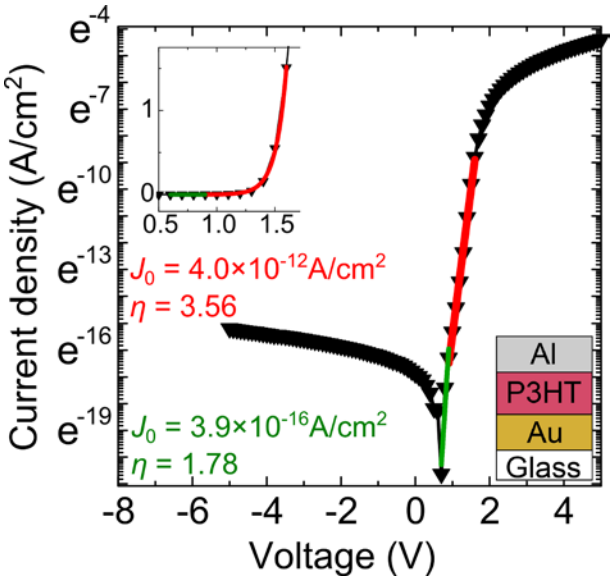

FIG. 7. log-linear ($\ln J-V$) plot for the OSDs along with device structure and device parameters (shown in inset) obtained from slopes of the linear regions and the inset represents the corresponding $J-V$ plot on linear scale which was fitted the thermionic equation model with J_0

obtained previously from $\ln J-V$ plot and the η were 1.81 and 3.54 in the lower (green) and higher (red) voltage range, respectively.

In OSDs, various types of physical phenomena occur in different region of the OSD as discussed in earlier section and their contribution in overall $J-V$ characteristic is also a function of voltage. Therefore, modeling of whole $J-V$ characteristic will be more reliable as compared to that of the linear part of the $\ln J-V$ plot only. In this regard, there are some reports, where the overall $J-V$ analysis has been done by integrating the sectional analysis using different physical phenomena or by considering one phenomenon and neglecting other.[7,24–28] For instance, in one of the analytical model proposed by Blom and coworkers, the effects of bulk and injection contacts were combined as drift (bulk effect) and diffusion (interface effect) contributions as a function of applied voltage.[28] The clear demarcation between the contributions of bulk and interface at certain applied voltage can lead to under estimation of their relative effect in some cases. Moreover, device structure dependent deviation of the physical model from practical electrical characteristics still remains a chalange.[26,29,30] However, being implicit function of voltage, the effective contribution of the physical phenomena in overall $J-V$ characteristic varies with applied bias. Which is also non-uniformly distributed in the whole device architecture as a function of regional/local non-linear resistances such as R_C and R_B. Thus, drawing a boundary between the effects of physical phenomena on voltage-scale/device-architecture seems improper since they can occur simultaneously. To address this issue, $J-V$ characteristic of any two terminal device can be interpreted through following relation,

$$J = \frac{V}{R_{\text{total}} \times a} \tag{5}$$

Where, $R_{\text{total}} = R_{\text{C}} + R_{\text{B}}$

Here *a* is the cross-sectional area of the device and R_{total} is the total resistance present in the device at any point of time and it consists of two parts, R_{C} and R_{B}. R_{C} and R_{B} are not simply Ohmic but they are also generated due to various non-Ohmic physical phenomena occurring in the device, such as band-bending due to charge accumulation, SCLS, trap states etc.[28] At lower forward bias ($V_{\text{a}} < V_{\text{bi}}$), the injection barrier at the Ohmic contact (here Au-P3HT contact) and at higher bias ($V_{\text{a}} > V_{\text{bi}}$) mainly SCLC governs the device $J-V$ characteristics. Scattering centers present at grain boundaries and trap states are exponentially distributed from contact towards the bulk and they contribute to both of the R_{C} and R_{B}, as shown in **Figure 8** (a – c). Thus, all the phenomena should be combined to frame an analytical model equation, where Ohmic and non-Ohmic part of R_{total} can be divided into three parts i.e. resistance due to nonlinear injection barrier, resistance due to SCLC and R_{series} (Ohmic loss throughout the device). Since trap states and scattering centers hamper the overall hole mobility thus their effect can be considered as R_{series} and effect of charge double layer can also be accounted in the same. The R_{C} and R_{B} are nonlinear function of voltage drops across contact and bulk of the OSD and in-situ measurement of these voltage distributions are not possible but macroscopic current density is same at any bias. Henceforth, interpreting their effect with current as a forcing function would provide an ease to interpret the effect of bulk and contact in one simple equation. Following our previous work, the analytical modeling equation is written with current as forcing function as Eq. 6.[62] For comparative study, some of the other equations as listed in **Table IV,** were also used to analyze the $J-V$ characteristics.[21,62]

$$V = \frac{\eta kT}{q}\ln\left(\frac{J}{J_0}+1\right) + \sqrt{\frac{8L^3J}{9\epsilon\epsilon_0\mu}} + JR_{\text{series}} \qquad (6)$$

Where, R_{series} is taken in the unit of 'Ωcm^2'.

L is the effective channel length, which is the film thickness in the present case (≈ 200 nm). ϵ and μ are relative permittivity and effective hole mobility with approximate values of 3 and 3×10^{-4} $cm^2V^{-1}s^{-1}$, respectively were taken from previous reports.[63,64]

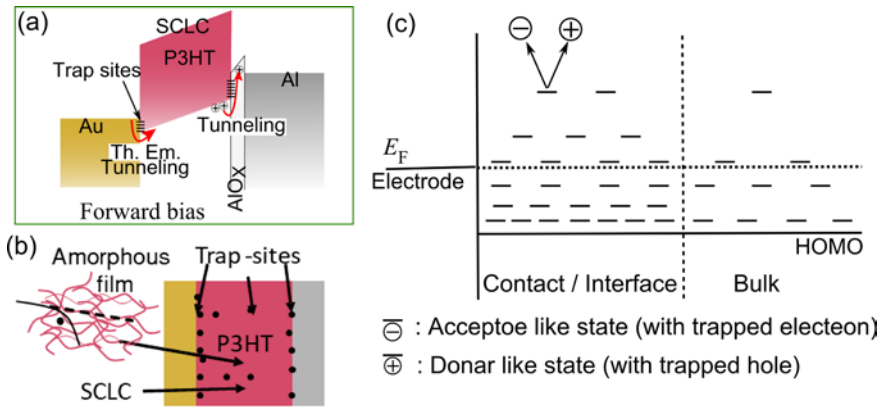

FIG. 8. (a) Energy band structure of the OSD (Al/P3HT/Au) in forward bias ($V_a > V_{bi}$) along with the physical different phenomena occurring in its different parts, (b) schematic representation for effect of trap sites in charge-scattering (the broken line represents the actual path of chrge flow in absence of scattering center or trap sites) and (c) Schematic illustration for exponential distribution of trap states in the device.

The experimental $J-V$ characteristics and the simulated models with different modeling equations (Table IV) are depicted in **Figure 9**. The constant/s J_0/(and η when kept constant) was/were obtained from the linear region (with lower slope as shown in Figure 7) of the $\ln J-V$ plot. The best fit of the experimental characteristics in different device architecture were analyzed through the simulated model based on Eq. 6 and the corresponding obtained device parameters are summarized in **Table V**. Hence Eq. 6 can be considered as general equation for the OSDs. As

already discussed, J_0 and η should be calculated from the low slope region of $J-V$ plot. To strengthen this discussion, comparison between the two linear regions (Figure 7) is also presented by fitting the experimental $J-V$ plots with the general analytical model (Eq. 6) as shown in **Figure S5**, where J_0 obtained from lower slope region fits better.

TABLE IV. The set of equations[21,62] followed for the comparative analysis of the experimental $J-V$ characteristics

Equation type	**Equation in mathematical form with J as forcing function; V(J)**	**Fitting Parameters**
Thermionic Emission (Th. Em.)	$V = \frac{\eta kT}{q} \ln\left(\frac{J}{J_0} + 1\right)$	η
Th. Em. + SCLC + Ohmic Loss(R_{series}); (constant η)	$V = \frac{\eta kT}{q} \ln\left(\frac{J}{J_0} + 1\right) + \sqrt{\frac{8L^3 J}{9\epsilon\epsilon_0\mu}} + JR_{\text{series}}$	R_{series}
Th. Em. + SCLC	$V = \frac{\eta kT}{q} \ln\left(\frac{J}{J_0} + 1\right) + \sqrt{\frac{8L^3 J}{9\epsilon\epsilon_0\mu}}$	η
Th. Em. + SCLC + Ohmic Loss(R_{series}); [Eq. 6]	$V = \frac{\eta kT}{q} \ln\left(\frac{J}{J_0} + 1\right) + \sqrt{\frac{8L^3 J}{9\epsilon\epsilon_0\mu}} + JR_{\text{series}}$	η, R_{series}

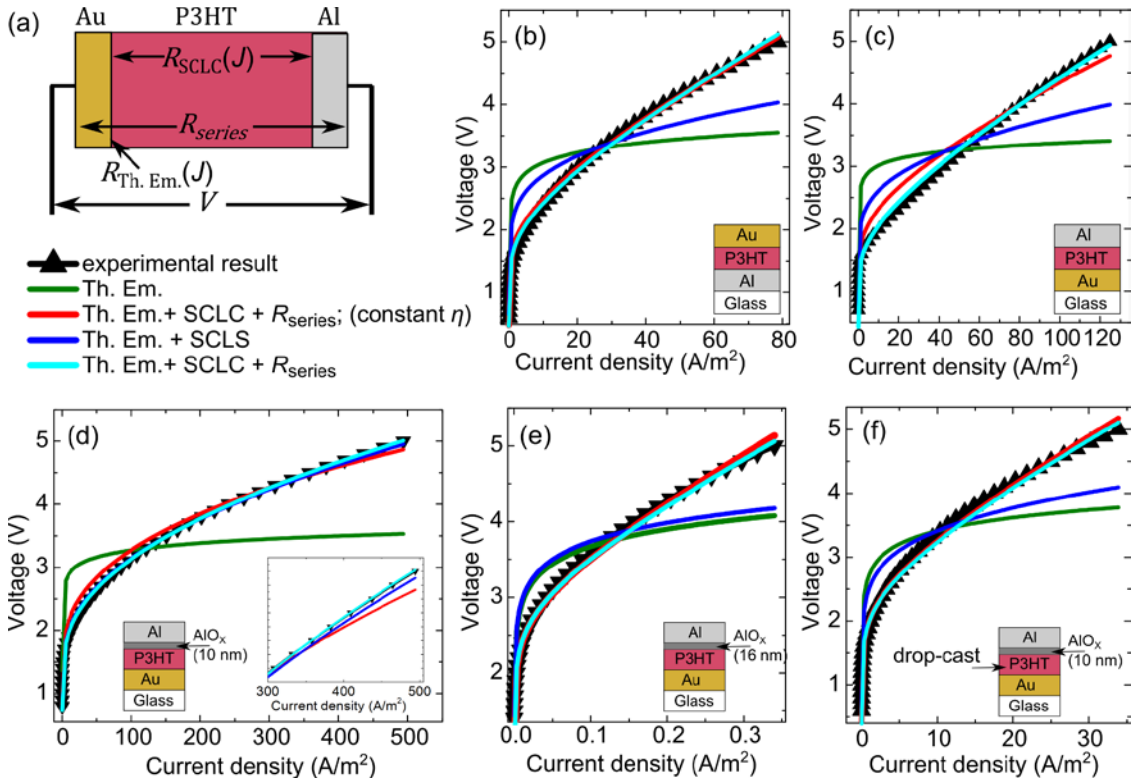

FIG. 9. (a) Schematic representation for occurrence of linear and nonlinear (function of J) resistance in different parts of the OSD (Al/P3HT/Au) and (b) set ligands for the experimental and fitted $J-V$ characteristics (c-g) the corresponding equations are written in Table 3. Inset of (e) represents the magnified part of fitted data at higher voltage. The constant values J_0 (and η only when mentioned) was (were) taken from partial linear fitting of $\ln J-V$ plot (Table 1,2 and Figure 7). The device structures are shown in the corresponding insets and all the OSDs were fabricated with spin-coated P3HT films except when it is mentioned.

Table V gives the understanding about the influence of metal/organic interfaces on the overall device resistance. The calculated value of R_{series} decreased by one order of magnitude in the case of 10 nm AlO_X interlayer as compared to that having only Al to make Schottky contact. On the other hand, it was of the same order in case of the bottom Al electrode and top Al electrode without AlO_X layer. In forward bias, at $V_a > V_{bi}$, space charge is being formed in the organic layer, which triggers tunneling of the charge carriers through the AlO_X layer. In addition to this, when charge double layer is closer to the film, tunneling will be speedup due to favorable Coulombic interaction.

At the same time, modified interfacial band structure due to AlO_X layer will be improving the charge transport, when it is near to the organic layer. The nanostructured AlO_X islands also improves the effective contribution of the charge-double layer. However, with increase in its thickness (for instance 16 nm), R_{series} increases due to the buried oxide layer, which is ineffective to support forward charge transport. This is also reflected in the obtained device parameters from fitted plot R_{series} (Table V) and the corresponding RR (Table I,III,SII). Precise observation in the case of 10 nm AlO_X interlayer shows that the experimental data is well fitted by the model without inclusion of R_{series}, however, inclusion of R_{series} provides better fit (Figure 9(e)). Unlike other cases, where the deviation is distinguishable due to the presence of comparatively lower R_{series}, this reduction can be attributed to favor the effective field due to charge double layer (Figure 3 (c)) and vice-versa in the case of Al as bottom contact.

TABLE V. Set of device parameters (η and R_{series}) obtained by fitting the experimental $J-V$ characteristics of different devices using Equation 6. The constant values of J_0 were taken from linear fitting of $\ln J-V$ plot (lower slope region, shown by red Figure 7). All the OSDs were fabricated with spin-coated P3HT films except when it is mentioned.

Device Structure	**Ideality factor (η)**	**R_{series} ($\Omega.cm^2$)**
Al (bottom contact)	2.84 ± 3.6%	844.6 ± 31.5%
Al (top contact) 0 nm AlO_X	2.95 ± 4.2%	113.6 ± 42.8%
Al (top contact) 10 nm AlO_X	3.54 ± 18.2%	32.7± 32.7%
Al (top contact) 16 nm AlO_X	15.63 ± 36.7%	3.39×10^5 ± 42.8%
Al (top contact) 10 nm AlO_X (P3HT drop-casted)	5.85 ± 24.5%	728.7 ± 30.0%

In order to demonstrate the application the OSDs in practical circuits, OSDs in device architecture exhibiting the best RR, was subjected to determine their maximum switching speed. For this measurement, the simplest circuit of a half-wave rectifier was designed. The OSD with dimension 100 µm × 500 µm (top Al contact and 10 nm of AlO_X interlayer) was connected in series with an AC-voltage source (V_{AC}) of a Function Generator and a load resistance (R_{Load}). The switching speed was obtained by comparing the output signal measured by an Oscilloscope across R_{Load} at varying input voltage frequency. By increasing the frequency of V_{AC} beyond maximum switching speed of the diode, it acts as a capacitor and cannot rectify the input signal. The maximum switching speed obtained for the test-OSD was 40 kHz as shown in **Figure S6** (supplementary information). It might be limited by the large displacement current from their capacitor behaver. To increase the switching speed further, the geometric configuration (cross-sectional area and film thickness) of the diode is currently under optimization and will be reported separately.[43] However, for other applications, where fast switching is not needed but significantly suppressed leakage current and high rectification ratio is desired, they can be better option, for instance to fabricated display backplanes with reduced crosstalk.[43]

IV. CONCLUSION

OSDs were fabricated using thin films of P3HT prepared by spin-coating and drop-casting methods in different device architectures. The implication of device architecture with the presence/absence of island deposited AlO_X interlayer on device performance has been investigated in detail using experimental data and analytical modeling. The metal/organic interface was

characterized through various techniques like XPS, UPS and AFM while nature of the organic thin film was characterized by GIXD. Here, application of AlO_X interlayer at the Schottky interface in order to enhance the RR of the OSDs was also successfully demonstrated. GIXD results revealed the edge conformation of P3HT for both of the spin coated and drop casted films, where, former exhibited relatively high crystallinity. Incorporation of 10 nm AlO_X interlayer in OSDs having top Al as Schottky contact led to the tremendous boost in the RR reaching > 10^6 at ± 5V. This enhancement was attributed to suppressed leakage current due to AlO_X interlayer at the Schottky interface as well as favored charge transport due to the formation of charge double layer. Furthermore, integration of equations pertaining to the various physical phenomena like thermionic emission and space charge limiting current led to the single general equation capable of modeling and interpretation of charge transport characteristics arising in OSDs fabricated in different architectures.

SUPPLEMENTARY INFORMATION

The $J-V$ characteristics for multiple device structure to represent the device to device statistical variation, the list of obtained device parameters, the optimization of AlO_X layer, the AFM image of AlO_X layer on bare SiO_2 substrate, the distribution map for AlO_X layer covering the underlying P3HT layer, comparison between J_0 obtained from different voltage region in terms of agreement between experimental and simulated $J-V$ characteristics, discussion and result of switching speed of the OSD.

ACKNOWLEDGMENT

One of the authors (NK) is thankful to Japan Student Services Organization and Kanazawa Memorial Foundation for supporting the research activity.

REFERENCES

[1] H. Klauk, Chem. Soc. Rev. **39**, 2643 (2010).
[2] K. Tremel and S. Ludwigs, Adv. Polym. Sci. **265**, 39 (2014).
[3] C. Adachi, Jpn. J. Appl. Phys. **53**, 060101 (2014).
[4] T. Berzina, K. Gorshkov, A. Pucci, G. Ruggeri, and V. Erokhin, RSC Adv. **1**, 1537 (2011).
[5] S. Lizin, S. Van Passel, E. De Schepper, W. Maes, L. Lutsen, J. Manca, and D. Vanderzande, Energy Environ. Sci. **6**, 3136 (2013).

[6] S. Holliday, Y. Li, and C.K. Luscombe, Prog. Polym. Sci. **70**, 34 (2017).
[7] C. Hyun Kim, O. Yaghmazadeh, Y. Bonnassieux, and G. Horowitz, J. Appl. Phys. **110**, 093722 (2011).
[8] S.D. Wang, T. Minari, T. Miyadera, K. Tsukagoshi, and J.X. Tang, Appl. Phys. Lett. **94**, 083309 (2009).
[9] S.D. Wang, T. Miyadera, T. Minari, Y. Aoyagi, and K. Tsukagoshi, Appl. Phys. Lett. **93**, 043311 (2008).
[10] W. Zhang, J. Smith, S.E. Watkins, R. Gysel, M. McGehee, A. Salleo, J. Kirkpatrick, S. Ashraf, T. Anthopoulos, M. Heeney, and I. McCulloch, J. Am. Chem. Soc. **132**, 11437 (2010).
[11] M.T. Greiner, M.G. Helander, W.M. Tang, Z. Bin Wang, J. Qiu, and Z.H. Lu, Nat. Mater. **11**, 76 (2012).
[12] S.D. Wang, T. Minari, T. Miyadera, K. Tsukagoshi, and Y. Aoyagi, Appl. Phys. Lett. **91**, 203508 (2007).
[13] P. V. Pesavento, K.P. Puntambekar, C.D. Frisbie, J.C. McKeen, and P.P. Ruden, J. Appl. Phys. **99**, 094504 (2006).
[14] C. Di, G. Yu, Y. Liu, Y. Guo, Y. Wang, W. Wu, and D. Zhu, Adv. Mater. **20**, 1286 (2008).
[15] K.E. Lilja, H.S. Majumdar, K. Lahtonen, P. Heljo, S. Tuukkanen, T. Joutsenoja, M. Valden, R. Sterbacka, and D. Lupo, J. Phys. D. Appl. Phys. **44**, 295301 (2011).
[16] M. Pandey, A. Gowda, S. Nagamatsu, S. Kumar, W. Takashima, S. Hayase, and S.S. Pandey, Adv. Mater. Interfaces **5**, 1700875 (2018).
[17] M. Pandey, S. Nagamatsu, S.S. Pandey, S. Hayase, and W. Takashima, Org. Electron. **38**, 115 (2016).
[18] M. Pandey, S. Nagamatsu, W. Takashima, S.S. Pandey, and S. Hayase, J. Phys. Chem. C **121**, 11184 (2017).
[19] R.R. Lunt, J.B. Benziger, and S.R. Forrest, Adv. Mater. **22**, 1233 (2010).
[20] M.A. Lampert and P. Mark, *Current Injection in Solids* (Academic Press, 1970).
[21] S.M. Sze and K.K. Ng, *Physics of Semiconductor Devices*, 3rd ed. (John Wiley & Sons, New Jersey, 2007).
[22] D. Braga, N. Battaglini, A. Yassar, G. Horowitz, M. Campione, A. Sassella, and A. Borghesi, Phys. Rev. B **77**, 115205 (2008).
[23] J. Sworakowski and K. Pigoń, J. Phys. Chem. Solids **30**, 491 (1969).
[24] M. Soylu, I.S. Yahia, F. Yakuphanoglu, and W.A. Farooq, J. Appl. Phys. **110**, 074514 (2011).
[25] M. Kuik, G.-J.A.H. Wetzelaer, H.T. Nicolai, N.I. Craciun, D.M. De Leeuw, and P.W.M. Blom, Adv. Mater. **26**, 512 (2014).
[26] A. Haldi, A. Sharma, W.J. Potscavage, and B. Kippelen, J. Appl. Phys. **104**, 064503 (2008).
[27] L.J.A. Koster, E.C.P. Smits, V.D. Mihailetchi, and P.W.M. Blom, Phys. Rev. B **72**, 085205 (2005).
[28] P. De Bruyn, A.H.P. Van Rest, G.A.H. Wetzelaer, D.M. De Leeuw, and P.W.M. Blom, Phys. Rev. Lett. **111**, 186801 (2013).
[29] P.W.M. Blom, C. Tanase, D.M. de Leeuw, and R. Coehoorn, Appl. Phys. Lett. **86**, 092105 (2005).
[30] H.T. Nicolai, G.A.H. Wetzelaer, M. Kuik, A.J. Kronemeijer, B. de Boer, and P.W.M. Blom, Appl. Phys. Lett. **96**, 172107 (2010).
[31] B.G. Streetman and S. Banerjee, *Solid State Electronic Devices*, 7th ed. (Oxford:Pearson, n.d.).
[32] H. Aziz, Z. Popovic, C.P. Tripp, N.-X. Hu, A.-M. Hor, and G. Xu, Appl. Phys. Lett. **72**, 2642 (1998).

[33] K. Kaneto and W. Takashima, Curr. Appl. Phys. **1**, 355 (2001).
[34] Y.I. Semov, Phys. Status Solidi **32**, K41 (1969).
[35] M.T. Greiner, L. Chai, M.G. Helander, W.M. Tang, and Z.H. Lu, Adv. Funct. Mater. **22**, 4557 (2012).
[36] V.K. Agarwala and T. Fort, Surf. Sci. **45**, 470 (1974).
[37] O. Güllü, S. Aydoğan, and A. Türüt, Solid State Commun. **152**, 381 (2012).
[38] B. Gunduz, I.S. Yahia, and F. Yakuphanoglu, in *Microelectron. Eng.* (2012), pp. 41–57.
[39] Y. Shi, S.-C. Luo, W. Fang, K. Zhang, E.M. Ali, F.Y.C. Boey, J.Y. Ying, J. Wang, H. Yu, and L.-J. Li, Org. Electron. **9**, 859 (2008).
[40] S.-W. Oh, H. Woo Rhee, C. Lee, Y. Chul Kim, J. Kyeong Kim, and J.-W. Yu, Curr. Appl. Phys. **5**, 55 (2005).
[41] A. Moliton and J.-M. Nunzi, Polym. Int. **55**, 583 (2006).
[42] C.J. Brabec, N.S. Sariciftci, and J.C. Hummelen, Adv. Funct. Mater. **11**, 15 (2001).
[43] T.M. Kraft, P.R. Berger, and D. Lupo, Flex. Print. Electron. **2**, 033001 (2017).
[44] C.H. Kim, O. Yaghmazadeh, D. Tondelier, Y. Bin Jeong, Y. Bonnassieux, and G. Horowitz, J. Appl. Phys. **109**, 083710 (2011).
[45] G. Gustafsson, O. Inganäs, M. Sundberg, and C. Svensson, Synth. Met. **41**, 499 (1991).
[46] T. Jiang, W. Malone, Y. Tong, D. Dragoe, A. Bendounan, A. Kara, and V.A. Esaulov, J. Phys. Chem. C **121**, 27923 (2017).
[47] V. Singh, A.K. Thakur, S.S. Pandey, W. Takashima, and K. Kaneto, Org. Electron. **9**, 790 (2008).
[48] Hong Wang, Zhuoyu Ji, Liwei Shang, Xinghua Liu, Yingquan Peng, and Ming Liu, IEEE Electron Device Lett. **31**, 506 (2010).
[49] C. Kang, S. Kim, Y. Hong, and C. Lee, Thin Solid Films **518**, 889 (2009).
[50] K.E. Lilja, H.S. Majumdar, F.S. Pettersson, R. Österbacka, and T. Joutsenoja, ACS Appl. Mater. Interfaces **3**, 7 (2011).
[51] S.G. Higgins, T. Agostinelli, S. Markham, R. Whiteman, and H. Sirringhaus, Adv. Mater. **29**, 1 (2017).
[52] J. Zhang, H. Wang, J. Wilson, X. Ma, J. Jin, and A. Song, IEEE Electron Device Lett. **37**, 389 (2016).
[53] A. Chasin, M. Nag, A. Bhoolokam, K. Myny, S. Steudel, S. Schols, J. Genoe, G. Gielen, and P. Heremans, IEEE Trans. Electron Devices **60**, 3407 (2013).
[54] S. Gupta, S. Hannah, C.P. Watson, P. Šutta, R.H. Pedersen, N. Gadegaard, and H. Gleskova, Org. Electron. **21**, 132 (2015).
[55] A. Wan, J. Hwang, F. Amy, and A. Kahn, Org. Electron. **6**, 47 (2005).
[56] M. Pandey, S.S. Pandey, S. Nagamatsu, S. Hayase, and W. Takashima, Org. Electron. **43**, 240 (2017).
[57] H. Yang, S.W. Lefevre, C.Y. Ryu, and Z. Bao, Appl. Phys. Lett. **90**, 172116 (2007).
[58] J.F. Chang, B. Sun, D.W. Breiby, M.M. Nielsen, T.I. Sölling, M. Giles, I. McCulloch, and H. Sirringhaus, Chem. Mater. **16**, 4772 (2004).
[59] R.D. Deegan, O. Bakajin, T.F. Dupont, G. Huber, S.R. Nagel, and T.A. Witten, Phys. Rev. E **62**, 756 (2000).
[60] J. Perelaer, P.J. Smith, E. Van Den Bosch, S.S.C. Van Grootel, P.H.J.M. Ketelaars, and U.S. Schubert, Macromol. Chem. Phys. **210**, 495 (2009).
[61] A.K. Singh, A.D.D. Dwivedi, P. Chakrabarti, and R. Prakash, J. Appl. Phys. **105**, 114506 (2009).
[62] A.K. Mukherjee and N. Kumari, Phys. Lett. A **382**, 1413 (2018).
[63] O. Armbruster, C. Lungenschmied, and S. Bauer, Phys. Rev. B **84**, 085208 (2011).

[64] S.A. Choulis, Y. Kim, J. Nelson, D.D.C. Bradley, M. Giles, M. Shkunov, and I. McCulloch, Appl. Phys. Lett. **85**, 3890 (2004).